

Conformal Tubular Parameterization and Toroidal Bending of Tube-Like Surfaces

Shunyu Yao¹, Gary P. T. Choi^{1,*}

¹Department of Mathematics, The Chinese University of Hong Kong, Hong Kong

*To whom correspondence should be addressed; E-mail: ptchoi@cuhk.edu.hk

Abstract

Tube-like surfaces are widely encountered in geometry processing, engineering structures, and medical anatomy, yet their intrinsic longitudinal and circumferential topology is not well preserved by conventional planar annular or rectangular parameterization domains. In this work, we propose a conformal parameterization framework for open tube-like surfaces with two boundary components. The proposed method first constructs a fixed-boundary tubular parameterization by cutting the input mesh, computing a disk-to-rectangle conformal map, and lifting the result to a three-dimensional tubular domain. To reduce residual distortion introduced near the cut seam, we further introduce a localized quasi-conformal correction scheme formulated on an annular domain, which improves conformality while leaving regions away from the seam unchanged. To handle noisy or irregular input boundaries, we also develop a free-boundary variant based on boundary extension and cycle-Laplacian smoothing, allowing the prescribed boundary constraints to be imposed on artificial outer rings rather than directly on the original surface. Finally, we derive two conformal toroidal bending maps that transform the tubular parameterization into toroidal geometries while preserving the underlying tube topology. Experiments on synthetic tube meshes and real vascular surfaces demonstrate that the proposed framework produces low-distortion parameterizations, effectively mitigates seam-induced artifacts, improves robustness for boundary-noisy inputs, and provides flexible tubular and toroidal target domains for downstream surface processing tasks.

1 Introduction

Surface parameterization maps a surface to a canonical domain and is a fundamental tool in computer graphics, geometry processing, visualization, and shape analysis. High-quality parameterizations facilitate tasks such as texture mapping, remeshing, shape comparison, and numerical computation on surfaces [1, 2]. Over the past several decades, a wide variety of surface parameterization methods have been developed, including barycentric and convex-combination mappings rooted in Tutte’s embedding theorem [3, 4], stretch-minimizing and near-isometric formulations such as MIPS (Most-Isometric ParameterizationS) [5], intrinsic and free-boundary methods [6], least-squares

conformal formulations such as LSCM (Least Squares Conformal Map) [7], angle-based methods such as ABF++ (Fast and Robust Angle Based Flattening) [8], local/global optimization frameworks [9], and injective parameterizations with explicit validity guarantees [10, 11].

Among the many available formulations, conformal parameterization is particularly attractive because it preserves angles and therefore retains local geometric structure. For instance, conformal parameterization has been widely used in texture mapping and automatic texture atlas generation [7, 12], in landmark-constrained surface registration and shape analysis [13], and in medical visualization tasks such as virtual colonoscopy and colon flattening for polyp detection [14, 15]. These applications highlight the practical value of conformal maps in situations where preserving local shape and controlling angular distortion are of primary importance. Notable examples also include cortical surface matching and brain surface mapping via conformal maps [16, 17].

Note that many recent parameterization methods focused on simply connected open surfaces [18, 19, 20, 21], genus-0 surfaces [22, 23, 24, 25, 26, 27, 28], or genus-1 surfaces [29, 30]. However, in practice, many surfaces exhibit tube topology. Representative examples include engineering structures such as pipelines, ducts, tunnels, and internal cooling channels, as well as medical structures such as blood vessels, bronchial trees, intestines, and other tubular anatomical organs. These examples suggest that tube-like surfaces are not exceptional cases but rather a common class of geometries in real-world applications. As a result, it is essential to design algorithms that can accurately represent, process, and analyze surfaces with tube topology.

A natural approach is to map these surfaces onto an annulus [31]. However, it is easy to see that flattening an elongated tube-like surface onto an annular planar domain may lead to significant geometric distortion, especially when the surface has a large aspect ratio or a highly nonuniform radius. Another possible approach is to cut the mesh open and map it onto a planar rectangular domain with periodic boundary conditions [32]. However, the artificial cut destroys the intrinsic cyclic structure of the surface, and maintaining periodic consistency across the two sides of the cut requires additional constraints and numerical effort. It is therefore natural to consider mapping tube-like surfaces onto more suitable target domains that preserve their topology while retaining a meaningful three-dimensional geometry.

In particular, tubular parameter domains provide a more faithful representation for surfaces with one dominant longitudinal direction and one periodic circumferential direction. Such target domains avoid the excessive radial distortion caused by annular flattening, while also eliminating the need to explicitly enforce periodic boundary matching after cutting. By respecting the intrinsic topology of tube-like surfaces, this type of parameterization can provide more stable and geometrically natural coordinates for downstream tasks such as texture mapping, remeshing, surface registration, shape analysis, and numerical simulation. A further possibility is to use a toroidally bent tube domain as an intermediate or alternative target domain. Instead of representing the parameter space as a straight cylinder, the tube is smoothly bent into a toroidal shape, preserving the periodic circumferential structure while allowing greater geometric flexibility along the longitudinal direction. This is particularly useful for tube-like surfaces whose centerlines are naturally curved, nearly closed, or ring-like, since the target domain can better reflect their global geometric structure without changing the underlying tubular topology.

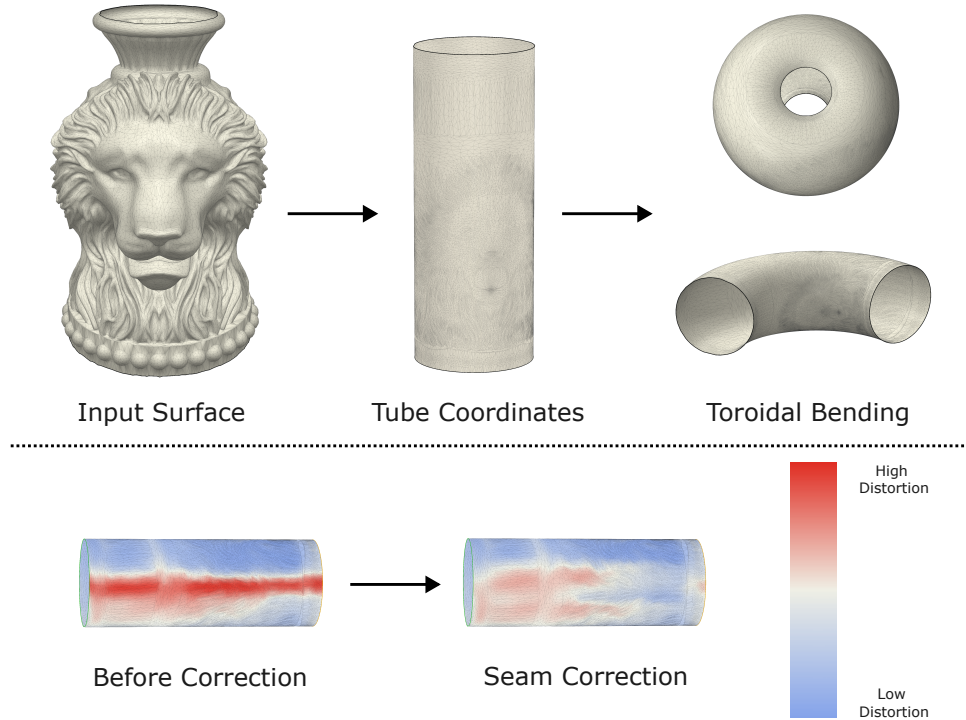


Figure 1: **Overview of the proposed conformal tubular parameterization and toroidal bending framework.** Top: an input tube-like surface is mapped to a tubular parameter domain and can then be conformally bent into toroidal geometries. Bottom: the localized seam correction reduces the distortion concentrated near the cut seam, as illustrated by the distortion heat map.

In this work, we propose a flexible conformal parameterization framework for tube-like surfaces (Fig. 1). Unlike planar annular or rectangular parameterizations, our method maps the input surface to tubular or toroidally bent tube domains that better respect the longitudinal and circumferential structure of tubular geometries. The main contributions of this work are threefold. First, we develop a fast tubular conformal parameterization method with customizable height, based on disk-to-rectangle conformal mapping and conformal lifting. Second, we introduce a localized quasi-conformal correction scheme to reduce seam-induced distortion while keeping the parameterization away from the seam unchanged. Third, we propose several domain-adaptive variants, including a free-boundary extension method for handling boundary variation and two conformal toroidal bending constructions for representing curved tube-like geometries. We validate the proposed methods on both synthetic examples and real medical vascular surfaces, and demonstrate their effectiveness in reducing distortion, improving boundary adaptability, and better fitting curved tubular shapes.

The rest of the paper is organized as follows. Section 2 presents the proposed conformal tubular parameterization framework, including the quasi-conformal preliminaries, the fixed-boundary tubular parameterization with localized seam correction, and the free-boundary extension variant. Section 3 introduces the conformal toroidal bending construction and the two associated bending modes. Section 4 evaluates the proposed

methods on synthetic and real vascular surfaces and reports ablation studies and computational cost. Section 5 concludes the paper and discusses possible future directions.

2 Conformal Tubular Parameterization

In this section, we introduce our proposed conformal tubular parameterization framework.

2.1 Quasi-conformal Map

We first briefly review the theoretical and computational aspects of quasi-conformal maps, which we use to control angular distortion in our parameterization problem.

Theory of quasi-conformal maps Let $f : \mathbb{C} \rightarrow \mathbb{C}$ be a complex-valued map

$$f(z) = f(x + iy) = u(x, y) + iv(x, y),$$

where u, v are real-valued C^1 functions. The map f is conformal if and only if it satisfies the Cauchy–Riemann equations:

$$\begin{cases} u_x = v_y, \\ u_y = -v_x. \end{cases} \quad (1)$$

A quasi-conformal map generalizes conformality by satisfying the Beltrami equation

$$f_{\bar{z}}(z) = \mu_f(z) f_z(z), \quad (2)$$

where

$$f_{\bar{z}} = \frac{1}{2}(f_x + if_y), \quad f_z = \frac{1}{2}(f_x - if_y),$$

and $\mu_f : \mathbb{C} \rightarrow \mathbb{C}$ is the Beltrami coefficient of f . When $\mu_f \equiv 0$, Eq. (2) reduces to Eq. (1). The Beltrami coefficient quantifies local angular distortion. For a quasi-conformal map with $|\mu_f| < 1$, the first fundamental form can be written as

$$I = Df^\top Df = |f_z|^2 Q^\top \begin{pmatrix} (1 + |\mu_f|)^2 & 0 \\ 0 & (1 - |\mu_f|)^2 \end{pmatrix} Q$$

for some orthonormal matrix Q . Hence, an infinitesimal circle centered at z is mapped to an infinitesimal ellipse centered at $f(z)$ (see Fig. 2) with principal stretches

$$\lambda_{\max} = |f_z(z)|(1 + |\mu_f(z)|), \quad \lambda_{\min} = |f_z(z)|(1 - |\mu_f(z)|).$$

The Beltrami coefficient of a composition also has a closed form. For compatible quasi-conformal maps f and g ,

$$\mu_{g \circ f} = \frac{\mu_f + (\bar{f}_z/f_z)(\mu_g \circ f)}{1 + (\bar{f}_z/f_z)\bar{\mu}_f(\mu_g \circ f)}.$$

If $\mu_g \equiv \mu_{f^{-1}}$, then $\mu_{g \circ f} = 0$ and $g \circ f$ is conformal. This observation is the basis for distortion correction via quasi-conformal composition.

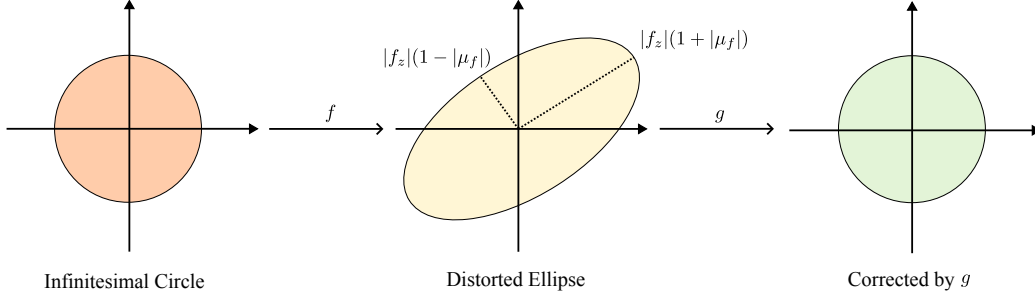


Figure 2: **Schematic illustration of distortion correction by quasi-conformal composition.** The map f transforms an infinitesimal circle into an ellipse with principal stretches $|f_z|(1 \pm |\mu_f|)$. Choose a quasi-conformal map g with $\mu_g \equiv \mu_{f^{-1}}$ cancels the anisotropy so that the composition satisfies $\mu_{g \circ f} = 0$.

Computation of quasi-conformal maps By the Measurable Riemann Mapping Theorem [33], a quasi-conformal map exists for any μ with $\|\mu\|_\infty < 1$. Based on this result, Lui et al. [34] introduced the Linear Beltrami Solver (LBS) method to compute $f = u + iv$ for a prescribed μ_f . From Eq. (2),

$$\frac{f_{\bar{z}}}{f_z} = \frac{(u_x - v_y) + i(v_x + u_y)}{(u_x + v_y) + i(v_x - u_y)},$$

which is equivalent to

$$\begin{pmatrix} \alpha_1 & \alpha_2 \\ \alpha_2 & \alpha_3 \end{pmatrix} \begin{pmatrix} u_x & v_x \\ u_y & v_y \end{pmatrix} = \begin{pmatrix} v_y & -u_y \\ -v_x & u_x \end{pmatrix}, \quad (3)$$

where

$$\alpha_1 = \frac{(\operatorname{Re}(\mu_f) - 1)^2 + \operatorname{Im}(\mu_f)^2}{1 - |\mu_f|^2}, \quad \alpha_2 = -\frac{2 \operatorname{Im}(\mu_f)}{1 - |\mu_f|^2}, \quad \alpha_3 = \frac{(\operatorname{Re}(\mu_f) + 1)^2 + \operatorname{Im}(\mu_f)^2}{1 - |\mu_f|^2}.$$

Using the differentiability of u and v , Eq. (3) leads to

$$\begin{cases} \nabla \cdot (A \nabla u) = 0, \\ \nabla \cdot (A \nabla v) = 0, \end{cases} \quad (4)$$

where $A = \begin{pmatrix} \alpha_1 & \alpha_2 \\ \alpha_2 & \alpha_3 \end{pmatrix}$. In the discrete setting, Eq. (4) reduces to two sparse symmetric positive-definite linear systems, which can be easily solved [34]. We denote the above linear Beltrami solving procedure by $f = \mathbf{LBS}(\mu_f)$.

2.2 Fixed-Boundary Conformal Parameterization

Given a connected triangulated open surface $M = (V, F)$ with exactly two boundary loops ∂M_0 and ∂M_1 , we construct a conformal tubular parameterization under fixed boundary constraints. The method comprises two stages: (i) initial tubular parameterization, and (ii) quasi-conformal correction.

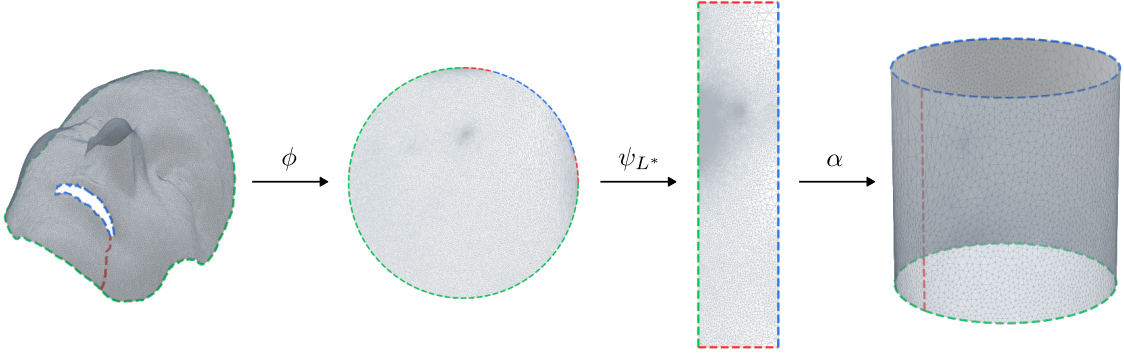


Figure 3: **Pipeline of the initial tubular parameterization.** Starting from an open surface with two boundary loops (colored in blue and green), we cut the mesh along a shortest cut path (colored in red), compute a disk harmonic map ϕ , conformally transform it to a rectangle via ψ_{L^*} , and then lift it to a 3D tube via α .

Initial tubular parameterization Our initial tubular parameterization builds on the rectangular conformal parameterization framework [32] and is lifted by a conformal lifting map (see Fig. 3).

We first cut M along a shortest boundary-to-boundary path γ to convert the annulus-topology mesh into a simply-connected mesh \widetilde{M} . This step is essential because the subsequent disk and rectangular parameterization is posed on simply-connected domains. Concretely, we construct a weighted graph $G = (V, E)$ from the mesh, where each edge $(v_i, v_j) \in E$ is assigned the Euclidean length $w_{ij} = \|v_i - v_j\|_2$. We then add two virtual source nodes, denoted by s_0 and s_1 where s_0 is connected to all vertices on ∂M_0 and s_1 is connected to all vertices on ∂M_1 using zero-weight edges. Running the Dijkstra’s algorithm [35] from s_0 to s_1 yields a geodesic-like discrete shortest path, which we take as the cut seam γ .

After obtaining a simply-connected mesh \widetilde{M} , we compute a disk harmonic map $\phi : \widetilde{M} \rightarrow \mathbb{D}$ by

$$\begin{cases} \Delta\phi = 0, \\ \phi(\partial\widetilde{M}) = \partial\mathbb{D}, \end{cases}$$

where the boundary values are set by arc-length parameterization. More concretely, let boundary vertices be $\{p_i\}_{i=1}^n$ in counterclockwise order, with edge lengths $\ell_i = \|p_{i+1} - p_i\|_2$ (cyclic indexing). We set

$$\theta_1 = 0, \quad \theta_i = 2\pi \frac{\sum_{j=1}^{i-1} \ell_j}{\sum_{j=1}^n \ell_j}, \quad i = 2, \dots, n,$$

and map each p_i to $(\cos \theta_i, \sin \theta_i)$. The Laplace operator Δ is discretized by the cotangent Laplacian L_{\cotan} with

$$(L_{\cotan})_{ij} = \begin{cases} \frac{1}{2A_i} (\cot \alpha_{ij} + \cot \beta_{ij}), & j \in \mathcal{N}_V(i), \\ -\frac{1}{2A_i} \sum_{k \in \mathcal{N}_V(i)} (\cot \alpha_{ik} + \cot \beta_{ik}), & j = i, \\ 0, & \text{otherwise,} \end{cases}$$

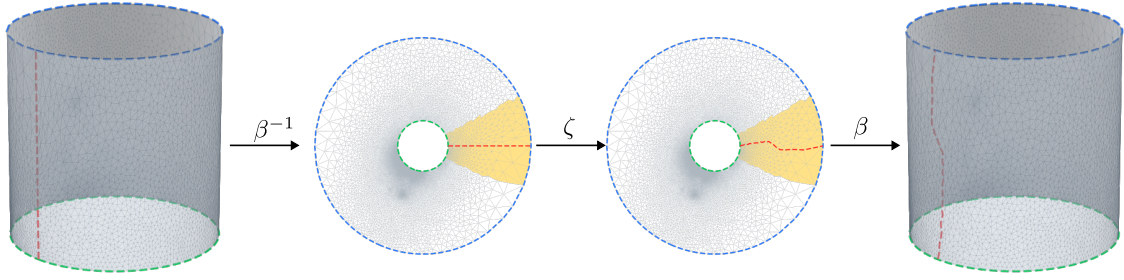


Figure 4: **Quasi-conformal correction for the initial tubular parameterization.** The initial tubular parameterization η is first transferred to the annulus \mathcal{A} via β^{-1} . A strip neighborhood (colored in yellow) of the cut seam is then corrected by a localized LBS map ζ , while the rest of the annulus is kept fixed. Finally, the corrected annulus parameterization is mapped back to the tube via β .

where $\mathcal{N}_V(i)$ denotes the one-ring vertex neighborhood of $v_i \in V$, α_{ij}, β_{ij} are the two angles opposite to edge (v_i, v_j) in the adjacent triangles and $A_i = \frac{1}{3} \sum_{T \in \mathcal{N}_F(i)} \text{Area}(T)$ is the area weight associated with v_i , with $\mathcal{N}_F(i)$ denoting the one-ring face neighborhood of v_i .

We then compute a quasi-conformal map $\psi_L : \mathbb{D} \rightarrow R_L = [0, 2\pi] \times [0, L]$ with target Beltrami coefficient

$$\psi_L = \mathbf{LBS}(\mu_{\phi^{-1}}).$$

Denote by p, p' the duplicated vertices at one endpoint of the cut path and by q, q' those at the other endpoint on $\partial \widetilde{M}$. We impose corner constraints

$$\begin{aligned} \psi_L(\phi(p)) &= (0, 0), & \psi_L(\phi(p')) &= (2\pi, 0), \\ \psi_L(\phi(q)) &= (0, L), & \psi_L(\phi(q')) &= (2\pi, L), \end{aligned}$$

and enforce periodic consistency for corresponding vertices on the two duplicated cut boundaries (same y -coordinates). We determine the optimal rectangle length L by

$$L^* = \arg \min_{L > 0} \|\mu_{\psi_L \circ \phi}\|^2.$$

After obtaining the rectangular parameterization $(u, z) \in R_L$, we map it to a standard tube $T = S^1 \times [0, L^*]$ via a conformal lifting map

$$\alpha(u, z) = (\cos(u), \sin(u), z),$$

and glue the cut path to reconstruct the tube topology. We denote the initial tubular parameterization map by $\eta = \alpha \circ \psi_{L^*} \circ \phi$.

Quasi-conformal correction η gives a high-quality initial tubular parameterization. Nevertheless, residual angular distortion may still be concentrated near the cut seam, and an additional correction step is therefore needed (see Fig. 4). Since correcting distortion directly on the tube geometry is nontrivial, we transfer the problem to an annulus, where

the correction can be formulated more conveniently [31]. Consider the conformal lifting map $\beta : \mathcal{A} \rightarrow T$ between the annulus $\mathcal{A} = \{w \in \mathbb{C} : 1 \leq |w| \leq e^{L^*}\}$ and the tube $T = S^1 \times [0, L^*]$, given by

$$\beta(w) = \left(\frac{\operatorname{Re}(w)}{|w|}, \frac{\operatorname{Im}(w)}{|w|}, \log |w| \right).$$

We then compute a localized angular-correction map on \mathcal{A} . Specifically, we only correct a narrow strip around the cut seam,

$$\mathcal{A}_d = \mathcal{A} \cap \{w \in \mathbb{C} : -d\pi \leq \arg(w) \leq d\pi\},$$

where $0 \leq d \leq 1$ controls the strip width, while the remaining region is kept unchanged. This localization is important because a global correction over the entire annulus may unnecessarily perturb areas that are already close to conformal and may introduce accumulated angular drift away from the seam. Let

$$\tilde{\mu}(w) = \begin{cases} \mu_{\eta^{-1} \circ \beta}(w), & w \in \mathcal{A}_d, \\ 0, & w \in \mathcal{A} \setminus \mathcal{A}_d. \end{cases}$$

On \mathcal{A}_d , we then solve

$$\zeta_d = \mathbf{LBS}(\tilde{\mu}),$$

with the boundary condition $\zeta_d(w) = w$ for all $w \in \partial\mathcal{A}_d$. The global correction map is defined by

$$\zeta(w) = \begin{cases} \zeta_d(w), & w \in \mathcal{A}_d, \\ w, & w \in \mathcal{A} \setminus \mathcal{A}_d. \end{cases}$$

By construction, ζ redistributes distortion only near the seam while leaving the rest of the annulus unchanged.

Finally, we map the corrected annulus parameterization back to the tube via β and compose all maps to obtain the fixed-boundary tubular parameterization:

$$\Phi_{\text{fix}} = \beta \circ \zeta \circ \beta^{-1} \circ \eta.$$

The complete fixed-boundary pipeline is summarized as

$$M \xrightarrow{\text{cut}} \widetilde{M} \xrightarrow{\phi} \mathbb{D} \xrightarrow{\psi_{L^*}} R_{L^*} \xrightarrow{\alpha} T \xrightarrow{\beta^{-1}} \mathcal{A} \xrightarrow{\zeta} \mathcal{A} \xrightarrow{\beta} T,$$

and Algorithm 1 summarizes the implementation details.

2.3 Free-Boundary Parameterization via Boundary Extension

Directly imposing circular boundary constraints on the original mesh may introduce boundary bias, particularly when the input boundaries are noisy or highly irregular. Inspired by virtual-boundary and scaffold-mesh techniques from early parameterization literature [36], we consider a free-boundary variant consisting of three steps (see Fig. 5): (i) raw extension of boundary loops, (ii) cycle-Laplacian smoothing, and (iii) restriction of the result back to the original surface.

Algorithm 1 Fixed-boundary conformal tubular parameterization

- 1: **Input:** Annulus-topology mesh $M = (V, F)$ with boundary loops $\partial M_0, \partial M_1$
 - 2: **Output:** Fixed-boundary tubular parameterization $\Phi_{\text{fix}} : M \rightarrow T$
 - 3: Build weighted graph G and find seam γ by Dijkstra between virtual sources linked to ∂M_0 and ∂M_1 .
 - 4: Cut M along γ to obtain simply-connected mesh \widetilde{M} .
 - 5: Compute harmonic disk map $\phi : \widetilde{M} \rightarrow \mathbb{D}$ with arc-length boundary constraints.
 - 6: Solve $\psi_L = \mathbf{LBS}(\mu_{\phi^{-1}})$ under corner/periodic constraints and optimize $L^* = \arg \min_{L>0} \|\mu_{\psi_L \circ \phi}\|^2$.
 - 7: Lift to initial tube by $\eta = \alpha \circ \psi_{L^*} \circ \phi$.
 - 8: Map to annulus via β^{-1} , solve a localized LBS correction on strip \mathcal{A}_d with fixed strip boundary and extend it by identity to obtain ζ .
 - 9: Return $\Phi_{\text{fix}} = \beta \circ \zeta \circ \beta^{-1} \circ \eta$.
-

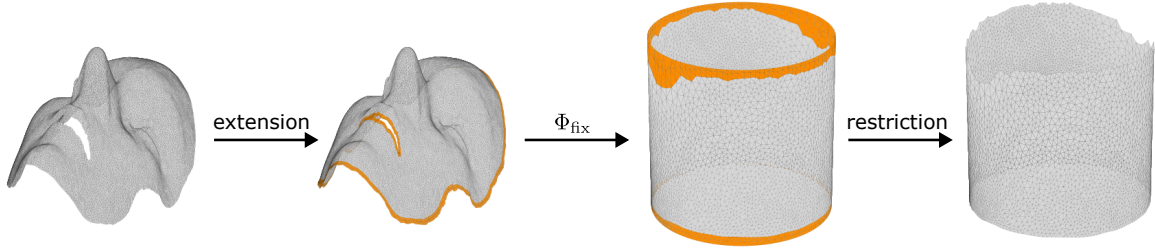


Figure 5: **Pipeline of the free-boundary tubular parameterization.** Boundary loops are extended and smoothed to form an augmented mesh M_{ext} (extended part is colored in orange), the fixed-boundary parameterization Φ_{fix} is applied on M_{ext} and the result is finally restricted back to the original mesh M .

Raw extension of boundary loops Let the two boundary loops be ∂M_0 and ∂M_1 . For each boundary loop, we iteratively append K triangle layers. At each iteration, we denote the current boundary ring by $\{\mathbf{p}_i\}_{i=1}^m$ (cyclic indexing) and define

$$\mathcal{N}_i^{\text{in}} = \{q \in \mathcal{N}_i : q \text{ is not on the current ring}\}.$$

We first compute the boundary tangent \mathbf{t}_i and an approximate inward direction \mathbf{u}_i (see Fig. 6):

$$\mathbf{t}_i = \frac{\mathbf{p}_{i+1} - \mathbf{p}_{i-1}}{\|\mathbf{p}_{i+1} - \mathbf{p}_{i-1}\|_2}, \quad \mathbf{u}_i = \frac{\sum_{q \in \mathcal{N}_i^{\text{in}}} (q - \mathbf{p}_i)}{\left\| \sum_{q \in \mathcal{N}_i^{\text{in}}} (q - \mathbf{p}_i) \right\|_2}.$$

A candidate lateral extension direction is given by

$$\tilde{\mathbf{b}}_i = \frac{\mathbf{t}_i \times \mathbf{n}_i}{\|\mathbf{t}_i \times \mathbf{n}_i\|_2},$$

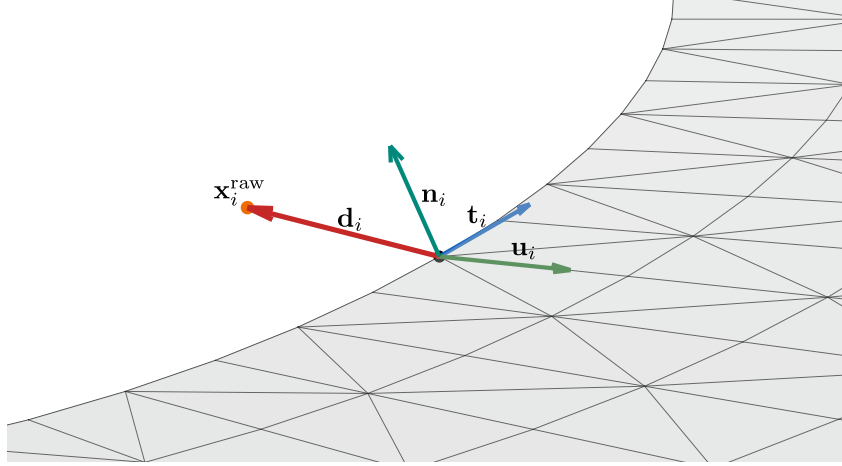


Figure 6: **Raw boundary extension on a boundary loop.** At each boundary vertex, an outward direction \mathbf{d}_i is estimated from local tangent \mathbf{t}_i , normal \mathbf{n}_i and inward \mathbf{u}_i .

where \mathbf{n}_i is an area-weighted incident face normal vector. Since $\tilde{\mathbf{b}}_i$ may point inward or outward depending on local orientation, we correct its sign by

$$\mathbf{b}_i = \begin{cases} -\tilde{\mathbf{b}}_i, & \text{if } \tilde{\mathbf{b}}_i \cdot \mathbf{u}_i > 0, \\ \tilde{\mathbf{b}}_i, & \text{otherwise.} \end{cases}$$

We then combine the lateral with normal components to improve robustness:

$$\mathbf{d}_i = \frac{(1 - \tau)\mathbf{b}_i + \tau\mathbf{n}_i}{\|(1 - \tau)\mathbf{b}_i + \tau\mathbf{n}_i\|_2},$$

where $\tau \in [0, 1]$ is the combination coefficient. The point-wise step length is estimated from the interior spacing

$$s_i = \frac{1}{|\mathcal{N}_i^{\text{in}}|} \sum_{q \in \mathcal{N}_i^{\text{in}}} \|q - \mathbf{p}_i\|_2.$$

Finally, the raw extension is given by

$$\mathbf{x}_i^{\text{raw}} = \mathbf{p}_i + \text{mean}(s_i)\mathbf{d}_i,$$

where we adopt the mean of all point-wise step lengths to reduce the influence of degenerate triangles near the boundary loops.

Cycle-Laplacian smoothing The raw extension is determined from local normals and local spacing and is therefore sensitive to uneven sampling and geometric noise. High-frequency zigzags may appear, leading to poorly shaped triangles and reduced stability in subsequent quasi-conformal correction on the original surface. We therefore formulate an energy minimization problem based on Laplacian smoothing [37] on the raw extension while keeping it close to the intended outward displacement (see Fig. 7 for an illustration). More specifically, we find the smoothed extension $\{\mathbf{x}_i\}_{i=1}^m$ (cyclic indexing) by minimizing the energy

$$E_{\text{smooth}} = \sum_{i=1}^m \|\mathbf{x}_i - \mathbf{x}_i^{\text{raw}}\|_2^2 + \omega \sum_{i=1}^m \|\mathbf{x}_{i+1} - \mathbf{x}_i\|_2^2,$$

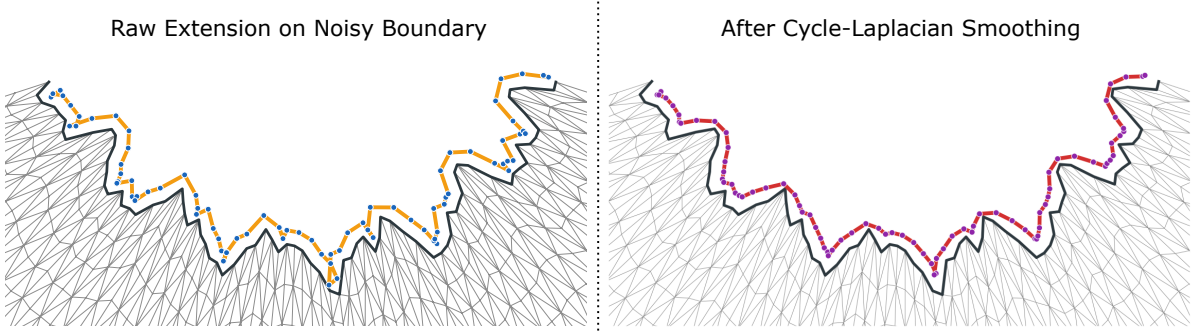


Figure 7: **Cycle-Laplacian smoothing of the raw extension.** The smoothed ring balances data fidelity, anchor regularization, and cycle smoothness, thereby suppressing high-frequency zigzags.

where ω is a weighting coefficient. This is a convex quadratic problem, and hence imposing the first-order optimality condition $\nabla E_{\text{smooth}} = 0$ yields a sparse symmetric linear system

$$(I + \omega L_{\text{cycle}}) \mathbf{x} = \mathbf{x}^{\text{raw}},$$

where the i -th row of $\mathbf{x} \in \mathbb{R}^{m \times 3}$ is \mathbf{x}_i (similarly for \mathbf{x}^{raw}) and L_{cycle} is the cycle-graph Laplacian matrix given by

$$(L_{\text{cycle}})_{ij} = \begin{cases} 2, & i = j, \\ -1, & j = i - 1 \text{ or } j = i + 1 \text{ in cyclic indexing,} \\ 0, & \text{otherwise.} \end{cases}$$

Restricting the result back to the original surface After extending both boundaries, we obtain an augmented mesh M_{ext} . We then apply the fixed-boundary pipeline in Section 2.2 to compute

$$\Phi_{\text{ext}} : M_{\text{ext}} \rightarrow T.$$

The final free-boundary parameterization on the original mesh is defined by

$$\Phi = \Phi_{\text{ext}}|_M.$$

Since explicit boundary constraints are imposed only on the artificial outer rings, the original boundaries are no longer forced onto prescribed circles, thereby reducing boundary bias while maintaining low angular distortion.

Algorithm 2 summarizes the procedure of free-boundary parameterization.

3 Conformal Tube Bending onto Toroidal Geometry

In the previous section, we established a methodology to obtain a tubular parameterization with low angular distortion for any open surface with two boundaries. We can further construct a bending map from the tube $T = S^1 \times [0, L]$ to a toroidal geometry

Algorithm 2 Free-boundary tubular parameterization via boundary extension

- 1: **Input:** Mesh M with boundary loops $\partial M_0, \partial M_1$, number of extension layers K , blending weight τ , smoothing weight ω
 - 2: **Output:** Free-boundary tubular parameterization $\Phi : M \rightarrow T$
 - 3: **for** each boundary loop ∂M_b , $b \in \{0, 1\}$ **do**
 - 4: **for** $k = 1, \dots, K$ **do**
 - 5: Estimate local directions $(\mathbf{t}_i, \mathbf{u}_i, \mathbf{n}_i)$, compute the oriented lateral direction \mathbf{b}_i , and set the outward direction as $\mathbf{d}_i = \frac{(1-\tau)\mathbf{b}_i + \tau\mathbf{n}_i}{\|(1-\tau)\mathbf{b}_i + \tau\mathbf{n}_i\|_2}$, for each vertex on the current boundary ring.
 - 6: Estimate the interior spacing s_i of each boundary vertex and compute raw ring points $\mathbf{x}_i^{\text{raw}} = \mathbf{p}_i + \bar{s}\mathbf{d}_i$, where $\bar{s} = \text{mean}_i(s_i)$.
 - 7: Solve the cycle-Laplacian smoothing system $(I + \omega L_{\text{cycle}})\mathbf{x} = \mathbf{x}^{\text{raw}}$ to obtain the smoothed ring $\{\mathbf{x}_i\}$.
 - 8: Stitch the smoothed ring to the mesh and update it as the current boundary loop.
 - 9: **end for**
 - 10: **end for**
 - 11: Obtain the augmented mesh M_{ext} after extending both boundary loops.
 - 12: Compute $\Phi_{\text{ext}} : M_{\text{ext}} \rightarrow T$ using Algorithm 1.
 - 13: Return $\Phi = \Phi_{\text{ext}}|_M$.
-

$\mathbb{T} = S^1 \times S^1$ while preserving conformality and topology. The final target map is a composition

$$\Psi = \mathcal{B} \circ \Phi,$$

where $\Phi : M \rightarrow T$ is the tubular parameterization and $\mathcal{B} : T \rightarrow \mathbb{T}$ is a conformal bending map.

Bending Formulation in Tube Coordinates Let a torus with major radius $R > 1$ and minor radius $r = 1$ be parameterized by

$$X(\theta, \phi) = ((R + \cos \theta) \cos \phi, (R + \cos \theta) \sin \phi, \sin \theta).$$

Its tangent vectors are

$$\begin{aligned} X_\theta &= (-\sin \theta \cos \phi, -\sin \theta \sin \phi, \cos \theta), \\ X_\phi &= -(R + \cos \theta) \sin \phi, (R + \cos \theta) \cos \phi, 0). \end{aligned}$$

Given tube coordinates (u, z) , we consider a general differentiable bending map

$$B(u, z) = X(\theta(u, z), \phi(u, z)).$$

Differentiating B gives

$$\begin{aligned} B_u &= X_\theta \theta_u + X_\phi \phi_u, \\ B_z &= X_\theta \theta_z + X_\phi \phi_z, \end{aligned}$$

and hence the first fundamental form is

$$ds^2 = E du^2 + 2F du dz + G dz^2,$$

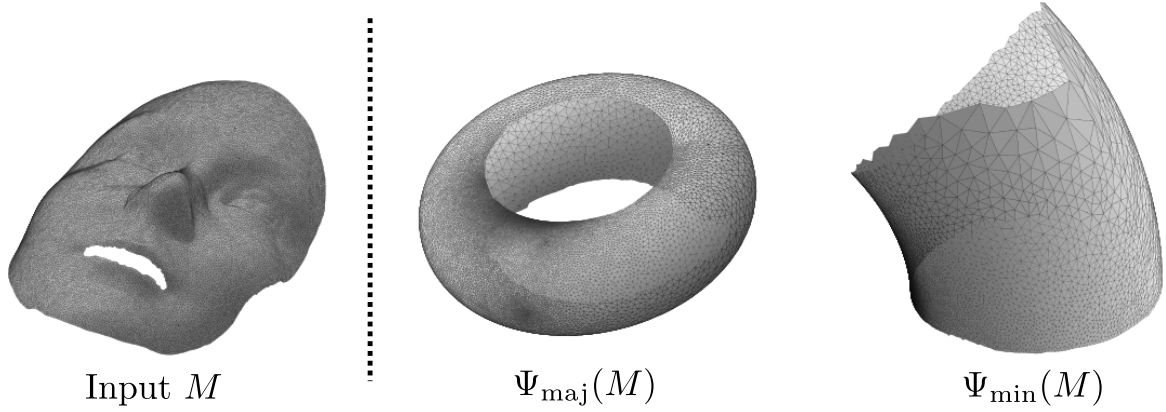


Figure 8: **Examples of conformal toroidal bending using the two different bending maps.** The results are obtained by full wrapping along the major circle Ψ_{maj} and full wrapping along the minor circle Ψ_{min} , respectively.

where

$$\begin{aligned} E &= \theta_u^2 + (R + \cos \theta)^2 \phi_u^2, \\ F &= \theta_u \theta_z + (R + \cos \theta)^2 \phi_u \phi_z, \\ G &= \theta_z^2 + (R + \cos \theta)^2 \phi_z^2. \end{aligned}$$

To construct a conformal bending map, we impose $E = G$ and $F = 0$ [38]. A tractable choice is to assume separated variables [39], e.g., $\theta = \theta(x)$ and $\phi = \phi(y)$, so that $F = 0$ automatically. The conformality condition then reduces to

$$\left(\frac{d\theta}{dx}\right)^2 = (R + \cos \theta)^2 \left(\frac{d\phi}{dy}\right)^2. \quad (5)$$

Since $R + \cos \theta > 0$ and the two sides of Eq. (5) depend on different variables, both sides must equal a constant c^2 with $c > 0$:

$$\left(\frac{1}{R + \cos \theta} \frac{d\theta}{dx}\right)^2 = \left(\frac{d\phi}{dy}\right)^2 = c^2.$$

Without loss of generality (up to orientation), we take

$$\frac{1}{R + \cos \theta} \frac{d\theta}{dx} = \frac{d\phi}{dy} = c.$$

Integrating with initial conditions $\theta(0) = 0$ and $\phi(0) = 0$ yields

$$\begin{cases} \theta(x) = 2 \arctan \left(\sqrt{\frac{R+1}{R-1}} \tan \left(\frac{\sqrt{R^2-1}}{2} cx \right) \right), \\ \phi(y) = cy. \end{cases}$$

We then obtain two bending maps by assigning x, y to u, z in two different ways (see Fig. 8), as detailed below.

Full Wrapping along the Major Circle We assign $x = z$ and $y = u$ so that

$$\begin{cases} \theta_{\text{maj}}(z) = 2 \arctan \left(\sqrt{\frac{R+1}{R-1}} \tan \left(\frac{\sqrt{R^2-1}}{2} c_{\text{maj}} z \right) \right), \\ \phi_{\text{maj}}(u) = c_{\text{maj}} u, \end{cases} \quad (6)$$

where $c_{\text{maj}} > 0$ is a constant associated with the major revolution. This assignment realizes a full wrapping along the major circle.

Since $u \in [0, 2\pi)$ is periodic, one complete wrapping around the major circle requires

$$\phi_{\text{maj}}(2\pi) - \phi_{\text{maj}}(0) = 2\pi.$$

Hence $c_{\text{maj}} = 1$, and Eq. (6) reduces to

$$\begin{cases} \theta_{\text{maj}}(z) = 2 \arctan \left(\sqrt{\frac{R+1}{R-1}} \tan \left(\frac{\sqrt{R^2-1}}{2} z \right) \right), \\ \phi_{\text{maj}}(u) = u. \end{cases}$$

The corresponding conformal bending map is

$$\mathcal{B}_{\text{maj}}(u, z) = \left((R + \cos \theta_{\text{maj}}(z)) \cos u, (R + \cos \theta_{\text{maj}}(z)) \sin u, \sin \theta_{\text{maj}}(z) \right),$$

with conformal factor

$$\lambda_{\text{maj}}(z) = R + \cos \theta_{\text{maj}}(z),$$

where the bending metric is $ds^2 = \lambda_{\text{maj}}(z)^2 (du^2 + dz^2)$. Since $R > 1$, we have $\theta'_{\text{maj}}(z) = R + \cos \theta_{\text{maj}}(z) > 0$ and hence the map is locally orientation-preserving without axial fold-over. Define

$$\Delta\theta_{\text{maj}} = \theta_{\text{maj}}(\max(z)) - \theta_{\text{maj}}(\min(z)),$$

which measures the meridional extent. To avoid wrap-around self-overlap in the minor direction, we impose

$$\Delta\theta_{\text{maj}} < 2\pi.$$

Set $\Delta z = \max(z) - \min(z)$. This condition can be enforced by choosing

$$R < \sqrt{1 + \left(\frac{2\pi}{\Delta z} \right)^2}. \quad (7)$$

The resulting full toroidal parameterization is

$$\Psi_{\text{maj}} = \mathcal{B}_{\text{maj}} \circ \Phi.$$

Full Wrapping along the Minor Circle Similarly, we assign $x = u$ and $y = z$, giving

$$\begin{cases} \theta_{\text{min}}(u) = 2 \arctan \left(\sqrt{\frac{R+1}{R-1}} \tan \left(\frac{\sqrt{R^2-1}}{2} c_{\text{min}} u \right) \right), \\ \phi_{\text{min}}(z) = c_{\text{min}} z, \end{cases} \quad (8)$$

where $c_{\text{min}} > 0$ is a constant associated with the minor revolution.

To enforce one complete cycle along the minor circle, we require

$$\theta_{\min}(2\pi) - \theta_{\min}(0) = 2\pi.$$

Using $\theta'(u) = c_{\min}(R + \cos \theta)$, we obtain

$$2\pi c_{\min} = \int_0^{2\pi} \frac{d\theta}{R + \cos \theta} = \frac{2\pi}{\sqrt{R^2 - 1}} \implies c_{\min} = \frac{1}{\sqrt{R^2 - 1}}.$$

Hence Eq. (8) becomes

$$\begin{cases} \theta_{\min}(u) = 2 \arctan \left(\sqrt{\frac{R+1}{R-1}} \tan \left(\frac{u}{2} \right) \right), \\ \phi_{\min}(z) = \frac{z}{\sqrt{R^2 - 1}}. \end{cases}$$

Therefore, the conformal bending map is

$$\mathcal{B}_{\min}(u, z) = \left((R + \cos \theta_{\min}(u)) \cos \phi_{\min}(z), (R + \cos \theta_{\min}(u)) \sin \phi_{\min}(z), \sin \theta_{\min}(u) \right),$$

with conformal factor

$$\lambda_{\min}(u) = \frac{R + \cos \theta_{\min}(u)}{\sqrt{R^2 - 1}}.$$

Since $\theta'_{\min}(u) = \frac{1}{\sqrt{R^2 - 1}}(R + \cos \theta_{\min}(u)) > 0$, the map is locally orientation-preserving. Moreover,

$$\Delta \phi_{\min} = \phi_{\min}(\max(z)) - \phi_{\min}(\min(z)) = \frac{\Delta z}{\sqrt{R^2 - 1}}$$

determines the major-direction coverage. To avoid wrap-around self-overlap in the major direction, we impose

$$\Delta \phi_{\min} < 2\pi.$$

This condition can be enforced by choosing

$$R > \sqrt{1 + \left(\frac{\Delta z}{2\pi} \right)^2}. \quad (9)$$

The resulting full toroidal parameterization is

$$\Psi_{\min} = \mathcal{B}_{\min} \circ \Phi.$$

The bending construction provides an alternative toroidal embedding of the tubular parameterization, and can be viewed as an optional conformal post-composition that switches the straight tube target domain to a toroidal one. The two resulting bending modes are complementary. In Ψ_{maj} , the axial coordinate is bent through the meridional direction of the torus while the periodic coordinate remains the major-circle parameter. In Ψ_{min} , the periodic coordinate is mapped to the minor-circle direction while the axial coordinate determines the progression along the major circle. The choice between the two modes can therefore be made according to whether the target application places greater emphasis on axial progression or on cross-sectional periodic structure. Algorithm 3 summarizes the final tube bending map.

Algorithm 3 Conformal tube bending

- 1: **Input:** Tubular parameterization $\Phi : M \rightarrow T$, major radius $R > 1$, mode $m \in \{\text{major}, \text{minor}\}$
 - 2: **Output:** Toroidal parameterization $\Psi : M \rightarrow \mathbb{T}$
 - 3: Compute $z_{\min} = \min(z)$ and $z_{\max} = \max(z)$ on $\Phi(M)$ and set $\Delta z = z_{\max} - z_{\min}$.
 - 4: Normalize $\hat{z} = z - \min(z)$.
 - 5: **if** $m = \text{major}$ **then**
 - 6: Choose $R < \sqrt{1 + \left(\frac{2\pi}{\Delta z}\right)^2}$ to avoid minor-direction overlap.
 - 7: Set $\theta(\hat{z}) = 2 \arctan\left(\sqrt{\frac{R+1}{R-1}} \tan\left(\frac{\sqrt{R^2-1}}{2} \hat{z}\right)\right)$ and $\phi(u) = u$.
 - 8: Define $\mathcal{B}_{\text{maj}}(u, z) = X(\theta(\hat{z}), \phi(u))$ and set $\Psi = \mathcal{B}_{\text{maj}} \circ \Phi$.
 - 9: **else**
 - 10: Choose $R > \sqrt{1 + \left(\frac{\Delta z}{2\pi}\right)^2}$ to avoid major-direction overlap.
 - 11: Set $\theta(u) = 2 \arctan\left(\sqrt{\frac{R+1}{R-1}} \tan\left(\frac{u}{2}\right)\right)$ and $\phi(\hat{z}) = \frac{\hat{z}}{\sqrt{R^2-1}}$.
 - 12: Define $\mathcal{B}_{\text{min}}(u, z) = X(\theta(u), \phi(\hat{z}))$ and set $\Psi = \mathcal{B}_{\text{min}} \circ \Phi$.
 - 13: **end if**
 - 14: Return Ψ
-

4 Experiments

4.1 Datasets and implementation details

We evaluate our proposed methods on both synthetic and real surface meshes (see Fig. 9). The synthetic benchmark contains 42 triangulated tube meshes generated procedurally from 4 geometry families: **straight**, **bent**, **tapered** and **wavy**. For each family, we add boundary noise to selected test cases.

The real dataset consists of 59 tube-like meshes derived from the Vascular Model Repository [40]. We restrict the collection to aortic and abdominal-aortic models and preprocess each case into a tube-like surface segment. The final set contains 40 aortic models and 19 abdominal-aortic models, with disease composition: 27 healthy cases, 13 abdominal aortic aneurysm cases, 6 coarctation-of-aorta cases, 6 Marfan syndrome cases, 5 single-ventricle-defect cases, and 2 aortoiliac occlusive disease cases.

All experiments are implemented in Python using NumPy, SciPy, trimesh, networkx. The estimated metric is the angular distortion in degrees. Unless otherwise specified, all benchmark runs use a seam-strip width of 0.05 for quasi-conformal correction and the cycle-Laplacian ring smoothing weight is set to $\omega = 0.5$ for free-boundary parameterization.

4.2 Evaluation of fixed-boundary conformal parameterization

We evaluate the localized quasi-conformal correction in the fixed-boundary pipeline by varying the seam-strip width d and explicitly including the no-correction baseline (Ta-

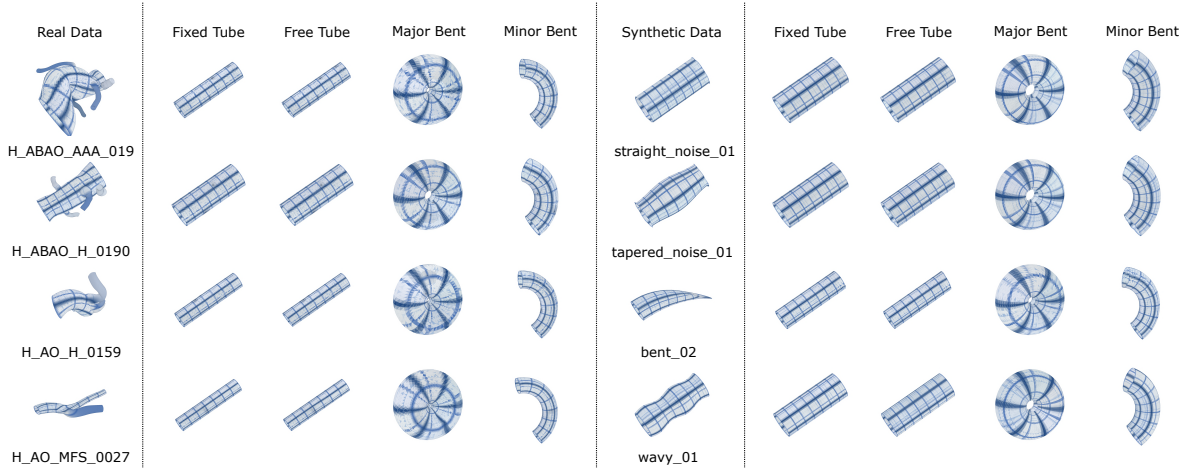


Figure 9: **Representative input surfaces and corresponding mapping results from the synthetic and real datasets.** Here, we illustrate several examples from a real vascular structure dataset (left) and a synthetic dataset (right), together with their parameterization results under the proposed framework.

ble 1). This unified experiment simultaneously serves as an ablation of the correction step and as a sensitivity analysis of the strip width.

On the synthetic benchmark, the no-correction baseline yields a mean distortion of 0.4024 and a median of 0.3491. Applying a narrow localized correction with $d = 0.05$ slightly reduces the mean distortion to 0.4001 while keeping the median essentially unchanged at 0.3492, and improves 30 out of 42 cases. A closer inspection indicates that the gain is concentrated on the boundary-noisy synthetic shapes: all 30 noisy cases are improved by $d = 0.05$, whereas the clean synthetic cases are already close to conformal after the initial tubular parameterization and hence exhibit only negligible changes. However, once the strip is enlarged, the distortion increases consistently. The mean distortion rises to 0.5104, 1.0612, and 1.9292 for $d = 0.25$, 0.45, and 0.65, respectively, and the corresponding medians increase to 0.3748, 0.4768, and 0.5028. This shows that, on synthetic shapes, the seam-induced error is highly localized and a wider correction region unnecessarily perturbs areas that are already well parameterized.

The same trend is more pronounced on the real vascular dataset. The no-correction baseline gives a mean distortion of 9.8582 and a median of 6.4523. Using $d = 0.05$ reduces these values to 9.7572 and 5.2924, respectively, and improves 50 out of 59 cases. In contrast, larger strip widths substantially degrade the parameterization quality: the mean distortion increases to 16.9941, 24.2948, and 32.1657 for $d = 0.25$, 0.45, and 0.65, while the median increases to 12.1552, 27.0287, and 28.9169. Moreover, the results for $d = 0.65$, 0.85, and 1.0 are nearly identical for all tested meshes, indicating that the method enters a saturated regime once the correction region becomes sufficiently wide. Overall, the best performance on both datasets is achieved by a narrow strip around the seam. Among all corrected settings, $d = 0.05$ gives the lowest distortion for 38 out of 42 synthetic cases and 49 out of 59 real cases. Therefore, the results support the design choice in Section 2.2: the residual distortion after the initial tubular parameterization is mainly seam-localized, and the quasi-conformal correction should remain localized as well.

d	Synthetic ($n = 42$)			Real ($n = 59$)		
	Mean	Median	Improved	Mean	Median	Improved
Init	0.4024	0.3491	–	9.8582	6.4523	–
0.05	0.4001	0.3492	30	9.7572	5.2924	50
0.25	0.5104	0.3748	4	16.9941	12.1552	7
0.45	1.0612	0.4768	1	24.2948	27.0287	5
0.65	1.9292	0.5028	2	32.1657	28.9169	3

Table 1: **Effect of the seam-strip width d on the fixed-boundary conformal parameterization.** “Init” denotes the initial tubular parameterization without localized quasi-conformal correction. Lower distortion is better. “Improved” denotes the number of cases whose distortion is lower than that of “Init”. The results for $d = 0.85$ and $d = 1.0$ are omitted for brevity since they are nearly identical to those for $d = 0.65$.

Based on this observation, we use $d = 0.05$ as the default strip width in all subsequent experiments.

4.3 Evaluation of free-boundary conformal parameterization

We evaluate the free-boundary parameterization in two aspects: (i) ablation of raw boundary extension and cycle-Laplacian smoothing, and (ii) the effect of the number of extension layers K .

We first isolate the effect of boundary extension itself by comparing the fixed-boundary baseline with the raw extension result, i.e., the free-boundary variant without cycle-Laplacian smoothing ($\omega = 0$). We then evaluate the additional contribution of cycle-Laplacian smoothing by varying $\omega > 0$ while fixing the number of extension layers to $K = 1$. The quantitative results are reported in Table 2.

On the synthetic benchmark, raw extension already improves the parameterization quality over the fixed-boundary baseline. Specifically, the mean distortion decreases from 0.4001 to 0.3820 and the median decreases from 0.3492 to 0.3112, and 32 out of 42 cases are improved. Adding cycle-Laplacian smoothing brings a further improvement. As ω increases, both the mean and median distortion decrease gradually, and the best overall result is attained at $\omega = 0.5$, for which the mean and median are reduced to 0.3746 and 0.3085, respectively. Compared with the fixed-boundary baseline, this corresponds to a total reduction of about 6.4% in the mean distortion and 11.6% in the median distortion. On the real vascular dataset, the trend is different. Raw extension does not improve the fixed-boundary baseline on average: the mean distortion increases from 9.7572 to 9.8422, and the median increases from 5.2924 to 5.3958. Applying cycle-Laplacian smoothing only partially regularizes this behavior. For example, with $\omega = 0.5$, the median decreases to 5.3093, but the mean distortion remains at 9.8450, which is still higher than the fixed-boundary baseline. Therefore, on the real dataset, the additional free-boundary processing does not bring a net improvement over the fixed-boundary pipeline.

The discrepancy between the synthetic and real datasets is likely due to the different boundary characteristics of the two benchmarks. In the synthetic benchmark, many test cases are generated with certain boundary perturbations, where the original boundary

Setting	Synthetic ($n = 42$)			Real ($n = 59$)		
	Mean	Median	Improved	Mean	Median	Improved
Fixed-boundary	0.4001	0.3492	–	9.7572	5.2924	–
Raw ext. ($\omega = 0$)	0.3820	0.3112	32	9.8422	5.3958	17
$\omega = 0.05$	0.3816	0.3106	32	9.8440	5.3957	17
$\omega = 0.10$	0.3812	0.3104	33	9.8460	5.3094	17
$\omega = 0.25$	0.3802	0.3097	33	9.8461	5.3093	16
$\omega = 0.50$	0.3746	0.3085	32	9.8450	5.3093	16

Table 2: Overall comparison of the fixed-boundary baseline, raw boundary extension, and smoothed free-boundary parameterization under different cycle-Laplacian weights ω . One extension layer is used for all free-boundary variants. Lower distortion is better. Improved denotes the number of cases whose distortion is lower than that of the fixed-boundary baseline.

loops can be noisy and irregular. In this setting, the free-boundary strategy is effective because the original noisy boundaries are no longer directly constrained to prescribed circles. The boundary extension step moves these constraints away from the original surface, and the subsequent cycle-Laplacian smoothing regularizes the extended rings, thereby reducing boundary-induced distortion and improving stability. By contrast, the real vascular meshes are preprocessed surface segments whose boundary loops are generally smoother and more regular. For these cases, the dominant error appears to be seam-localized residual distortion rather than boundary bias, and this error is already well handled by the localized correction in the fixed-boundary pipeline.

To make this observation more explicit, we further split the synthetic benchmark into clean and boundary-noisy subsets according to the procedural data generation; see Table 3. The gain of the free-boundary method is indeed stronger on the noisy subset. For the noisy cases, the mean distortion decreases from 0.4441 for the fixed-boundary baseline to 0.4227 after raw extension and further to 0.4126 with $\omega = 0.5$. By contrast, for the clean cases, the corresponding values are 0.2902, 0.2802, and 0.2795, indicating a smaller improvement margin. This supports the interpretation that the main benefit of the free-boundary pipeline is to reduce boundary bias when the input boundaries are noisy. A more direct verification of this hypothesis would be to quantify boundary roughness and correlate it with the performance gap between the fixed-boundary and free-boundary methods, which we leave for future work.

We next examine the effect of the number of extension layers K using the default smoothing weight $\omega = 0.5$; see Table 4. On the synthetic benchmark, $K = 1$ gives the best overall mean distortion 0.3746, while increasing the number of layers to $K = 2$ and $K = 3$ raises the mean distortion to 0.4107 and 0.4258, respectively. Although $K = 2$ yields a slightly smaller median than $K = 1$ (0.3007 versus 0.3085), its worse mean distortion and smaller number of improved cases indicate that deeper extension reduces robustness overall. On the real dataset, the degradation is monotone: the mean and median distortion increase from 9.8450 and 5.3093 at $K = 1$ to 9.9779 and 5.4453 at $K = 2$ and 10.0973 and 5.6173 at $K = 3$. Moreover, among the tested layer numbers, $K = 1$ achieves the lowest distortion for 26 out of 42 synthetic cases and 44 out of 59 real cases. Therefore, one extension

Setting	Clean ($n = 12$)			Noisy ($n = 30$)		
	Mean	Median	Improved	Mean	Median	Improved
Fixed-boundary	0.2902	0.2556	–	0.4441	0.3729	–
Raw ext. ($\omega = 0$)	0.2802	0.2417	4	0.4227	0.3522	28
$\omega = 0.50$	0.2795	0.2411	6	0.4126	0.3486	26

Table 3: Breakdown of the synthetic benchmark into clean and boundary-noisy subsets. The comparison focuses on the fixed-boundary baseline, raw extension, and the default smoothed setting $\omega = 0.5$. Lower distortion is better. Improved denotes the number of cases whose distortion is lower than that of the fixed-boundary baseline within the corresponding subset.

K	Synthetic ($n = 42$)				Real ($n = 59$)			
	Mean	Median	Improved	Best	Mean	Median	Improved	Best
1	0.3746	0.3085	32	26	9.8450	5.3093	16	44
2	0.4107	0.3007	26	7	9.9779	5.4453	13	1
3	0.4258	0.3064	20	9	10.0973	5.6173	14	14

Table 4: Effect of the number of extension layers K in the free-boundary parameterization. The smoothing weight is fixed at $\omega = 0.5$. Lower distortion is better. Improved denotes the number of cases whose distortion is lower than that of the fixed-boundary baseline. Best denotes the number of cases for which a given K attains the lowest distortion among all tested layer numbers.

layer is sufficient in practice, whereas adding more layers tends to accumulate geometric perturbation without bringing consistent conformality gains.

Overall, the experiments suggest that the free-boundary strategy is mainly useful when the input boundaries are unreliable. On the synthetic benchmark, raw extension already improves the results, and cycle-Laplacian smoothing further enhances robustness. On the real vascular dataset, however, the fixed-boundary formulation remains preferable on average. Taking both accuracy and simplicity into account, we use $K = 1, \omega = 0.5$ as the default setting in the remaining experiments whenever the free-boundary variant is considered.

4.4 Evaluation of conformal tube bending

We evaluate the conformal tube bending in two aspects: (i) comparison between the two bending maps Ψ_{maj} and Ψ_{min} , and (ii) the sensitivity of the bending distortion to the torus major radius within the theoretically admissible regime. Since the admissible range of R is different for the two bending modes, we do not sweep R directly. Instead, we parameterize the radius by two dimensionless variables, ρ_{maj} and ρ_{min} .

For the major-radius bending map Ψ_{maj} , using the upper-bound condition in Eq. (7), we define

$$R_\rho = 1 + \rho_{\text{maj}} \left(\sqrt{1 + \left(\frac{2\pi}{\Delta z} \right)^2} - 1 \right).$$

where $\rho_{\text{maj}} = 1$ corresponds to the theoretical upper bound, and all reported results satisfy $\rho_{\text{maj}} < 1$.

For the minor-radius bending map Ψ_{min} , using the lower-bound condition in Eq. (9), we define

$$R_\rho = \rho_{\text{min}} \sqrt{1 + \left(\frac{\Delta z}{2\pi}\right)^2}.$$

where $\rho_{\text{min}} = 1$ corresponds to the theoretical lower bound, and all reported results satisfy $\rho_{\text{min}} > 1$.

The default fixed-boundary tubular parameterization is used as the baseline before bending, where the mean and median tube distortion is 0.4001 and 0.3492 on the synthetic benchmark and 9.7572 and 5.2924 on the real vascular dataset. The quantitative results are reported in Tables 5 and 6.

Comparing the two bending modes, Ψ_{min} consistently preserves conformality better than Ψ_{maj} within the theoretically admissible regime. On the synthetic benchmark, the best tested Ψ_{maj} result is attained at $\rho_{\text{maj}} = 0.99$, with mean and median distortion 1.1913 and 1.1553, respectively, whereas the best tested Ψ_{min} result is attained at $\rho_{\text{min}} = 5.0$, with mean and median distortion 0.4639 and 0.4120. Relative to the tube baseline, this corresponds to an additional mean distortion of 0.7912 for Ψ_{maj} but only 0.0638 for Ψ_{min} . The same tendency is observed on the real vascular dataset. The best tested Ψ_{maj} result gives mean and median distortion 9.8304 and 5.3354, whereas the best tested Ψ_{min} result gives 9.7624 and 5.2924. Comparing these two best settings on a case-by-case basis, Ψ_{min} yields lower distortion for all 42 synthetic cases and for 58 out of 59 real cases. Therefore, when minimizing the additional distortion introduced by toroidal bending is the main objective, Ψ_{min} is the preferable default choice.

It is worth noting that the conformal bending map in Section 3 is derived in the smooth setting. In particular, if the bending map were evaluated exactly on the smooth tube surface, then post-composition by a conformal map would not change the local angular distortion already present in the tubular parameterization. Therefore, the fact that the bent results in Tables 5 and 6 still exhibit additional distortion should be understood as a discrete effect rather than a contradiction of the continuous theory. More specifically, the tube map Φ is computed numerically on a triangulated mesh and is therefore only approximately conformal on the discrete surface. In addition, the toroidal bending map is nonlinear in the tube coordinates, whereas the bent surface is represented by piecewise-linear triangles after moving the mesh vertices. As a result, each smooth toroidal image patch is approximated by a chordal triangle in \mathbb{R}^3 , and the measured per-face angular distortion contains a discretization error. This error becomes more pronounced when the torus is more tightly curved, namely when the tested radius is close to its theoretical bound, and becomes smaller as the admissible radius increases. Irregular sampling and nonuniform triangle quality can further amplify this effect on triangulated meshes in practice.

Consistent with the above interpretation, larger admissible radii reduce the measured distortion for both bending modes. For Ψ_{maj} , increasing ρ_{maj} from 0.01 to 0.99 monotonically decreases both the mean and median distortion on the synthetic and real datasets. The setting $\rho_{\text{maj}} = 0.99$ gives the lowest distortion among all tested major-mode settings, and it is also the best setting for all 42 synthetic cases and for 58 out of 59 real cases.

ρ_{maj}	Synthetic ($n = 42$)		Real ($n = 59$)	
	Mean	Median	Mean	Median
Tube	0.4001	0.3492	9.7572	5.2924
0.01	1.4943	1.4901	9.8650	5.3644
0.10	1.4741	1.4689	9.8621	5.3617
0.20	1.4494	1.4450	9.8588	5.3587
0.40	1.3935	1.3898	9.8518	5.3526
0.60	1.3296	1.3187	9.8445	5.3466
0.80	1.2597	1.2352	9.8371	5.3408
0.99	1.1913	1.1553	9.8304	5.3354

Table 5: Effect of the control parameter ρ_{maj} on the full-wrapping-along-major-circle bending map Ψ_{maj} . The torus major radius is parameterized by $R_\rho = 1 + \rho_{\text{maj}} \left(\sqrt{1 + \left(\frac{2\pi}{\Delta z}\right)^2} - 1 \right)$ according to the upper-bound condition in Eq. (7). Only theoretically admissible values with $\rho_{\text{maj}} < 1$ are reported. Lower distortion is better. The row “Tube” denotes the tubular parameterization before bending.

This is consistent with the construction in Section 3: increasing ρ_{maj} moves the radius closer to the largest admissible value allowed by Eq. (7), thereby weakening the bending while remaining within the valid regime.

For Ψ_{min} , increasing ρ_{min} from 1.01 to 5.0 also monotonically decreases both the mean and median distortion. The near-threshold setting $\rho_{\text{min}} = 1.01$ produces substantially larger distortion, especially on the synthetic benchmark, showing that bending remains relatively strong when the radius is chosen too close to the lower bound in Eq. (9). As ρ_{min} increases, the bent parameterization becomes progressively closer to the original tubular parameterization. Among all tested minor-mode settings, $\rho_{\text{min}} = 5.0$ gives the lowest distortion for all 42 synthetic cases and for 49 out of 59 real cases. Overall, the experiments show that larger admissible radii are beneficial for both bending modes, and that Ψ_{min} consistently remains closer to the original tubular parameterization than Ψ_{maj} .

4.5 Summary of ablation study and computational cost

Taken together, the ablation results suggest a clear practical configuration of the proposed framework. For the fixed-boundary pipeline, the residual distortion after the initial tubular parameterization is predominantly seam-localized, and hence the quasi-conformal correction should remain localized as well. A narrow strip with $d = 0.05$ gives the best overall trade-off on both datasets, whereas enlarging the correction region unnecessarily perturbs already well-parameterized areas and substantially increases angular distortion. For the free-boundary pipeline, the main benefit is observed when the input boundaries are noisy or unreliable, namely when boundary bias is a more important source of error than seam-localized residual distortion. In practice, a shallow extension is sufficient: one extension layer together with moderate smoothing achieves the best overall balance, while deeper extension tends to accumulate geometric perturbation without bringing consistent conformality gains.

For conformal tube bending, Ψ_{min} consistently remains closer to the original tubular parameterization than Ψ_{maj} within the admissible regime. Moreover, for both bending

ρ_{\min}	Synthetic ($n = 42$)		Real ($n = 59$)	
	Mean	Median	Mean	Median
Tube	0.4001	0.3492	9.7572	5.2924
1.01	1.0372	0.9935	9.8176	5.3084
1.50	0.7299	0.6686	9.7862	5.2982
2.00	0.6195	0.5571	9.7757	5.2952
2.50	0.5619	0.5046	9.7705	5.2939
3.00	0.5266	0.4746	9.7675	5.2933
4.00	0.4861	0.4368	9.7641	5.2927
5.00	0.4639	0.4120	9.7624	5.2924

Table 6: Effect of the control parameter ρ_{\min} on the full-wrapping-along-minor-circle bending map Ψ_{\min} . The torus major radius is parameterized by $R_{\rho} = \rho_{\min} \sqrt{1 + \left(\frac{\Delta z}{2\pi}\right)^2}$ according to the lower-bound condition in Eq. (9). All reported values satisfy $\rho_{\min} > 1$. Lower distortion is better. The row “Tube” denotes the tubular parameterization before bending.

modes, larger admissible radii reduce the measured distortion on triangulated meshes. Therefore, when minimizing the additional distortion introduced by toroidal bending is the primary objective, Ψ_{\min} with a relatively large admissible radius is the preferred default choice.

To complement the distortion-based ablation, we also record the runtime of the default free-boundary pipeline, namely raw boundary extension, cycle-Laplacian smoothing, initial tubular parameterization, localized seam correction, and restriction back to the original surface, together with the two optional bending maps; see Table 7. The average total runtime is 0.4801 s per synthetic mesh (median 0.4446 s) and 3.5306 s per real mesh (median 2.9209 s). The higher cost on the real dataset is consistent with its larger average mesh resolution (22972 versus 5669 vertices). Across both datasets, the initial tubular parameterization is by far the dominant cost, accounting for 89.4% of the total runtime on the synthetic benchmark and 93.6% on the real dataset. By comparison, the localized seam correction contributes only 2.2% and 1.3% respectively. The extra overhead introduced by the free-boundary module is modest: raw boundary extension and cycle-Laplacian smoothing together account for about 8.3% of the total runtime on the synthetic benchmark and 5.0% on the real dataset, while the restriction step is negligible. The computational cost of the two toroidal bending maps is also negligible compared with that of the parameterization stage. Overall, the proposed framework is computationally practical for moderate-resolution tube-like meshes, and the main bottleneck lies in the core parameterization solve rather than in the boundary extension module or the final bending map.

5 Conclusion and discussion

In this work, we proposed a conformal parameterization framework for tube-like surfaces together with a conformal bending construction onto toroidal geometry. For open surfaces with two boundary loops, we first developed a fixed-boundary tubular parameterization

Stage	Synthetic ($n = 42$)		Real ($n = 59$)	
	Mean	Median	Mean	Median
Total pipeline	0.4801	0.4446	3.5306	2.9209
Raw extension	0.0341 (7.1%)	0.0306	0.1537 (4.4%)	0.1516
Cycle-Laplacian smoothing	0.0056 (1.2%)	0.0051	0.0238 (0.7%)	0.0236
Initial tubular parameterization	0.4291 (89.4%)	0.3965	3.3052 (93.6%)	2.6578
Localized seam correction	0.0108 (2.2%)	0.0099	0.0457 (1.3%)	0.0343
Restriction	9.25×10^{-7}	9.54×10^{-7}	1.07×10^{-6}	9.54×10^{-7}
Ψ_{maj} bending	2.50×10^{-4}	2.42×10^{-4}	1.09×10^{-3}	1.01×10^{-3}
Ψ_{min} bending	2.33×10^{-4}	2.15×10^{-4}	1.10×10^{-3}	9.91×10^{-4}

Table 7: Computation time breakdown of the default free-boundary pipeline and the two optional toroidal bending maps. All times are reported in seconds. Percentages in parentheses denote the fraction of the mean total pipeline time.

method that combines an initial tube map with a localized quasi-conformal correction around the cut seam. To further reduce boundary bias caused by noisy or irregular input boundaries, we introduced a free-boundary variant based on boundary extension, cycle-Laplacian smoothing, and restriction back to the original surface. Building on the resulting tube coordinates, we then derived conformal bending maps that transform the tube into a toroidal geometry while preserving topology and conformality in the smooth setting.

A central message of this study is that the dominant source of parameterization distortion depends on the geometric characteristics of the input surface. When the boundaries are relatively regular, the main error is typically seam-localized residual distortion, for which the fixed-boundary formulation with localized correction is already effective. When the boundaries are noisy or unreliable, boundary bias becomes more significant, and the free-boundary formulation becomes advantageous because it moves the imposed boundary constraints away from the original surface. In this sense, the fixed-boundary and free-boundary variants should be viewed as complementary rather than universally competing choices.

The toroidal bending results also highlight an important distinction between the smooth theory and its discrete realization on triangulated meshes. In the smooth setting, post-composition by a conformal bending map does not introduce new angular distortion. In practice, however, the tubular parameterization is computed numerically on a discrete mesh, and the nonlinear toroidal image is represented by piecewise-linear triangles after vertex relocation. The measured post-bending distortion should therefore be interpreted as a discretization effect rather than a contradiction of the continuous conformal theory. This also explains why weaker bending and better mesh quality lead to smaller observed distortion in the experiments. From a practical viewpoint, the straight tube should remain the distortion-oriented baseline, while toroidal bending serves as a low-overhead optional toroidal embedding when a toroidal target domain is desired.

Several directions remain for future work. First, it would be useful to design an adaptive criterion for automatically choosing between the fixed-boundary and free-boundary formulations, for example by quantifying boundary roughness and relating it to the expected boundary bias. Second, since the discrepancy after bending is mainly discrete, more accu-

rate discretizations of the bending step and mesh-quality-aware formulations may further improve performance on irregularly sampled surfaces. Third, although the current implementation is already practical for moderate-resolution meshes, further acceleration of the core parameterization stage would be valuable. Finally, it would be interesting to extend the framework to more general tubular geometries and to downstream applications such as geometry processing, medical shape analysis, and surface remeshing.

References

- [1] M. S. Floater and K. Hormann, “Surface parameterization: a tutorial and survey,” in *Advances in Multiresolution for Geometric Modelling* (N. A. Dodgson, M. S. Floater, and M. A. Sabin, eds.), (Berlin, Heidelberg), pp. 157–186, Springer Berlin Heidelberg, 2005.
- [2] A. Sheffer, E. Praun, and K. Rose, “Mesh parameterization methods and their applications,” *Found. Trends Comput. Graph. Vis.*, vol. 2, no. 2, pp. 105–171, 2006.
- [3] W. T. Tutte, “How to draw a graph,” *Proc. London Math. Soc.*, vol. s3-13, no. 1, pp. 743–767, 1963.
- [4] M. S. Floater, “Parametrization and smooth approximation of surface triangulations,” *Comput. Aided Geom. Des.*, vol. 14, no. 3, pp. 231–250, 1997.
- [5] K. Hormann and G. Greiner, “MIPS: An efficient global parametrization method,” in *Curve and Surface Design: Saint-Malo 1999* (P.-J. Laurent, P. Sablonnière, and L. L. Schumaker, eds.), pp. 153–162, Nashville, TN: Vanderbilt University Press, 2000.
- [6] M. Desbrun, M. Meyer, and P. Alliez, “Intrinsic parameterizations of surface meshes,” *Comput. Graph. Forum*, vol. 21, no. 3, pp. 209–218, 2002.
- [7] B. Lévy, S. Petitjean, N. Ray, and J. Maillot, “Least squares conformal maps for automatic texture atlas generation,” *ACM Trans. Graph.*, vol. 21, no. 3, pp. 362–371, 2002.
- [8] A. Sheffer, B. Lévy, M. Mogilnitsky, and A. Bogomyakov, “ABF++: fast and robust angle based flattening,” *ACM Trans. Graph.*, vol. 24, no. 2, p. 311–330, 2005.
- [9] L. Liu, L. Zhang, Y. Xu, C. Gotsman, and S. J. Gortler, “A local/global approach to mesh parameterization,” in *Proceedings of the Symposium on Geometry Processing, SGP '08*, (Goslar, DEU), pp. 1495–1504, Eurographics Association, 2008.
- [10] O. Weber and D. Zorin, “Locally injective parametrization with arbitrary fixed boundaries,” *ACM Trans. Graph.*, vol. 33, no. 4, 2014.
- [11] M. Rabinovich, R. Poranne, D. Panozzo, and O. Sorkine-Hornung, “Scalable locally injective mappings,” *ACM Trans. Graph.*, vol. 36, no. 4, p. 1, 2017.

- [12] S. Haker, S. Angenent, A. Tannenbaum, R. Kikinis, G. Sapiro, and M. Halle, “Conformal surface parameterization for texture mapping,” *IEEE Trans. Vis. Comput. Graph.*, vol. 6, no. 2, pp. 181–189, 2000.
- [13] L. M. Lui, S. Thiruvankadam, Y. Wang, P. M. Thompson, and T. F. Chan, “Optimized conformal surface registration with shape-based landmark matching,” *SIAM J. Imaging Sci.*, vol. 3, no. 1, pp. 52–78, 2010.
- [14] W. Hong, X. Gu, F. Qiu, M. Jin, and A. Kaufman, “Conformal virtual colon flattening,” in *Proceedings of the 2006 ACM Symposium on Solid and Physical Modeling, SPM '06*, (New York, NY, USA), pp. 85–93, Association for Computing Machinery, 2006.
- [15] S. Haker, S. B. Angenent, A. R. Tannenbaum, and R. Kikinis, “Nondistorting flattening maps and the 3-D visualization of colon CT images,” *IEEE Trans. Med. Imaging*, vol. 19, pp. 665–670, 2000.
- [16] X. Gu, Y. Wang, T. Chan, P. Thompson, and S.-T. Yau, “Genus zero surface conformal mapping and its application to brain surface mapping,” *IEEE Trans. Med. Imaging*, vol. 23, no. 8, pp. 949–958, 2004.
- [17] Y. Wang, L. M. Lui, X. Gu, K. M. Hayashi, T. F. Chan, A. W. Toga, P. M. Thompson, and S.-T. Yau, “Brain surface conformal parameterization using Riemann surface structure,” *IEEE Trans. Med. Imaging*, vol. 26, no. 6, pp. 853–865, 2007.
- [18] R. Sawhney and K. Crane, “Boundary first flattening,” *ACM Trans. Graph.*, vol. 37, no. 1, 2017.
- [19] G. P. T. Choi, Y. Leung-Liu, X. Gu, and L. M. Lui, “Parallelizable global conformal parameterization of simply-connected surfaces via partial welding,” *SIAM J. Imaging Sci.*, vol. 13, no. 3, pp. 1049–1083, 2020.
- [20] W.-H. Liao and M.-H. Yueh, “A constructive algorithm for disk conformal parameterizations,” *J. Sci. Comput.*, vol. 92, no. 2, p. 40, 2022.
- [21] G. P. T. Choi and M. Shaqfa, “Hemispheroidal parameterization and harmonic decomposition of simply connected open surfaces,” *J. Comput. Appl. Math.*, vol. 461, p. 116455, 2025.
- [22] S. Nadeem, Z. Su, W. Zeng, A. Kaufman, and X. Gu, “Spherical parameterization balancing angle and area distortions,” *IEEE Trans. Vis. Comput. Graph.*, vol. 23, no. 6, pp. 1663–1676, 2016.
- [23] X. Hu, X.-M. Fu, and L. Liu, “Advanced hierarchical spherical parameterizations,” *IEEE Trans. Vis. Comput. Graph.*, vol. 24, no. 6, pp. 1930–1941, 2017.
- [24] Z. Wang, Z. Luo, J. Zhang, and E. Saucan, “A novel local/global approach to spherical parameterization,” *J. Comput. Appl. Math.*, vol. 329, pp. 294–306, 2018.

- [25] W.-H. Liao, T.-M. Huang, W.-W. Lin, and M.-H. Yueh, “Convergence of Dirichlet energy minimization for spherical conformal parameterizations,” *J. Sci. Comput.*, vol. 98, no. 1, p. 29, 2024.
- [26] G. P. T. Choi, “Fast ellipsoidal conformal and quasi-conformal parameterization of genus-0 closed surfaces,” *J. Comput. Appl. Math.*, vol. 447, p. 115888, 2024.
- [27] M. Sutti and M.-H. Yueh, “Riemannian gradient descent for spherical area-preserving mappings,” *AIMS Math.*, vol. 9, no. 7, p. 19414, 2024.
- [28] Z. Lyu, L. M. Lui, and G. P. T. Choi, “Spherical density-equalizing map for genus-0 closed surfaces,” *SIAM J. Imaging Sci.*, vol. 17, no. 4, pp. 2110–2141, 2024.
- [29] M.-H. Yueh, T. Li, W.-W. Lin, and S.-T. Yau, “A new efficient algorithm for volume-preserving parameterizations of genus-one 3-manifolds,” *SIAM J. Imaging Sci.*, vol. 13, no. 3, pp. 1536–1564, 2020.
- [30] S. Yao and G. P. T. Choi, “Toroidal density-equalizing map for genus-one surfaces,” *J. Comput. Appl. Math.*, vol. 472, p. 116844, 2026.
- [31] G. P. T. Choi, “Efficient conformal parameterization of multiply-connected surfaces using quasi-conformal theory,” *J. Sci. Comput.*, vol. 87, no. 3, p. 70, 2021.
- [32] T. W. Meng, G. P.-T. Choi, and L. M. Lui, “TEMPO: Feature-endowed Teichmüller extremal mappings of point clouds,” *SIAM J. Imaging Sci.*, vol. 9, no. 4, pp. 1922–1962, 2016.
- [33] L. Ahlfors and L. Bers, “Riemann’s mapping theorem for variable metrics,” *Ann. Math.*, vol. 72, no. 2, pp. 385–404, 1960.
- [34] L. M. Lui, K. C. Lam, T. W. Wong, and X. Gu, “Texture map and video compression using Beltrami representation,” *SIAM J. Imaging Sci.*, vol. 6, no. 4, pp. 1880–1902, 2013.
- [35] E. W. Dijkstra, “A note on two problems in connexion with graphs,” *Numer. Math.*, vol. 1, no. 1, p. 269–271, 1959.
- [36] R. Zayer, C. Rössl, and H.-P. Seidel, “Setting the boundary free: a composite approach to surface parameterization,” in *Proceedings of the Third Eurographics Symposium on Geometry Processing*, SGP ’05, (Goslar, DEU), p. 91–es, Eurographics Association, 2005.
- [37] G. Taubin, “A signal processing approach to fair surface design,” in *Proceedings of the 22nd Annual Conference on Computer Graphics and Interactive Techniques*, SIGGRAPH ’95, (New York, NY, USA), pp. 351–358, Association for Computing Machinery, 1995.
- [38] X. Gu and S.-T. Yau, “Global Conformal Surface Parameterization,” in *Eurographics Symposium on Geometry Processing* (L. Kobbelt, P. Schroeder, and H. Hoppe, eds.), The Eurographics Association, 2003.

- [39] N.-E. Guenther, P. Massignan, and A. L. Fetter, “Superfluid vortex dynamics on a torus and other toroidal surfaces of revolution,” *Phys. Rev. A*, vol. 101, p. 053606, 2020.
- [40] N. M. Wilson, A. K. Ortiz, and A. B. Johnson, “The vascular model repository: A public resource of medical imaging data and blood flow simulation results,” *J. Med. Devices*, vol. 7, no. 4, p. 040923, 2013.